$CH_3NH_3PbI_3$ and $CH_3NH_3PbBr_3$ films deposited by automated spray-pyrolysis for applications in photovoltaic energy

T. M. S. Fernandes[1]*, H. R. Paes Junior[1]

[1]*State University of Northern Rio de Janeiro Darcy Ribeiro, Advanced Materials Laboratory, 28013-602, Av. Alberto Lamego 2000, Campos dos Goytacazes, RJ, Brazil*

Abstract

This work aimed to produce $CH_3NH_3PbI_3$ and $CH_3NH_3PbBr_3$ films on glass substrates via the automated spray-pyrolysis technique for application as an absorber layer of photovoltaic cells. Their properties were investigated and compared by varying deposition parameters, such as the temperature (250, 300, 350, and 400 °C) and the precursor solution flow (0.25, 0.50, and 0.75 mL/min). Structural characterization by X-ray diffraction revealed the formation of orthorhombic perovskite films. The most adequate temperature and solution flow were 300 °C and 0.50 mL/min for both bromine and iodide films. Morphologically, the films were uniform and free from cracks. $CH_3NH_3PbI_3$ and $CH_3NH_3PbBr_3$ films respectively had an optical gap of 1.5 and 2.3 eV, a thickness of 4.56 and 2.35 μm, an absorption coefficient of 0.58×10^4 and 0.50×10^4 cm^{-1}, a resistivity of 21.80 and 24.20 kΩ.m, and a figure of merit of 2.66 and 2.07. It was concluded that, between the two compounds, the $CH_3NH_3PbI_3$ layer has better performance for photovoltaic applications.

Keywords: solar cell, perovskite, spray-pyrolysis.

INTRODUCTION

The ceramic mineral calcium titanate discovered in 1839 by Rouse was named perovskite in honor of the mineralogist Perovski. Since then, this nomenclature has been used to identify other mineral structures with the same atomic arrangement [1]. In 2009, perovskite-based solar cells of lead methylammonium iodide ($CH_3NH_3PbI_3$ or $MAPbI_3$) and lead methylammonium bromide ($CH_3NH_3PbBr_3$ or $MAPbBr_3$) were developed, demonstrating a solar energy-to-electrical energy conversion efficiency of 3.81% and 3.13%, respectively [2]. However, in the past 10 years, their efficiency has increased to 25.7%, which is comparable to silicon-based solar cells that currently dominate the market [3]. Despite the recent research investigating alternative forms of perovskite [4, 5], the decision to focus on the pioneering compounds is justified by their extensive coverage in the literature since their discovery in 2009 [6]. These materials have emerged as prominent candidates for the next generation of photovoltaic technology, due to their unique properties. They demonstrate high absorption coefficients, and notably, they can be synthesized using simple solution-based methods, which is an appealing feature for the development of low-cost solar cells [6]. Perovskite-based solar cells are semitransparent and flexible, unlike the silicon-based ones, which are opaque. Thus, they can be installed not only on roofs or in solar power plants distant from the consumer unit, but also on glass surfaces (e.g., solar roofs, car/residential/building windows), which can function as energy generators [7].

The most used method for $MAPbI_3$ and $MAPbBr_3$ film deposition is spin-coating [1, 2, 3, 6, 7]. However, it is not efficient for large-scale commercialization purposes or large-area coverage due to its significant waste material [6]. $MAPbI_3$ and $MAPbBr_3$ perovskite layers had not yet been produced via the automated spray-pyrolysis (ASP) deposition technique. Therefore, there is a need to produce both types of films via the ASP technique and assess their performance to determine which is better. In this perspective, this study proposes to investigate and optimize the deposition of $MAPbI_3$ and $MAPbBr_3$ perovskite layers on a glass substrate using spray pyrolysis deposition for use as a photon absorber layer in photovoltaic devices. The chosen technique is simple, low-cost, scalable to large areas, and allows for the possibility of depositing all cell layers in the same equipment in the future [8-10]. The production of $MAPbI_3$ and $MAPbBr_3$ films aimed to investigate the effects of spray pyrolysis deposition parameters, such as temperature and precursor solution flow rate, on the morphological, optical, electrical, and structural properties of the films. The quality of the films produced via ASP was evaluated aiming to optimize the device for future studies.

MATERIALS AND METHODS

The substrate was a smooth and transparent glass slide, commonly employed in microscopic analysis, that was precisely cut and meticulously cleaned to facilitate its fitting in the automated spray-pyrolysis (ASP) deposition system. To obtain the precursor solutions, the reagents were calculated by stoichiometry, diluted in the dimethylformamide (DMF) solvent (99.8% purity), and magnetically stirred for 40 min. Lead iodide (PbI_2, powder, 99.0% purity)

**thaismasouz@gmail.com*
https://orcid.org/0009-0007-3485-0256

and methylammonium iodide (MAI, factory-diluted in 2-propanol) were used for MAPbI$_3$, while lead bromide (PbBr$_2$, powder, purity ≥98.0%) and methylammonium bromide (MABr, factory-diluted in 2-propanol) were used for MAPbBr$_3$ [9]. All products were purchased from Sigma Aldrich.

ASP was the deposition method used to produce the films. The precursor solution, containing ions of interest, was sprayed through a carrier gas. The micro-droplet underwent pyrolysis when falling onto the substrate positioned on top of a heated plate. Eventually, it is expected to form the desired final compound [8, 10]. The film properties were investigated under the effect of the deposition parameters as follows: temperature of the heating plate (250, 300, 350, and 400 °C), precursor solution flow rate (0.25, 0.50, and 0.75 mL/min), deposition time of 5 min, atomizer nozzle positioned at 30 cm from the substrate, a gas pressure of 0.5 kgf/cm², and precursor solution concentration of 0.025 M.

Morphological characterization was carried out on each sample to investigate potential cracks and heterogeneities via topographic analysis using a confocal microscope (OLS 4000, Olympus). Film thickness was determined through cross-sectional analysis which consisted of measuring the thickness at multiple points along the cross-section and then obtaining an average value. Optical characterization was conducted using a dual-beam spectrophotometer (UV-1800 Shimadzu), which measured the absorption of light from 350 to 1000 nm, with a reference at 700 nm. The absorption coefficient (α) of the films was determined using the transmittance (T) equation [11]:

$$T = \frac{I}{I_0} = \exp^{(-\alpha x)} \qquad (A)$$

where I is the intensity of the incident radiation, I$_0$ is the intensity of the radiation that passes through the film, and x is the film thickness. Rearranging the equation with respect to α, we obtain [11]:

$$\alpha = \frac{\ln\left(\frac{1}{T}\right)}{x} \qquad (B)$$

After calculating the α values, the Tauc graph, (αhν)^2 by photon energy (hν), was plotted, where, h is Planck's constant and ν is the frequency. The optical gap value (E$_g$) of the films was determined by linear extrapolation of the curves [11]. The electrical characterization was carried out by measuring the variation in electrical conductivity (σ) as a function of temperature (T). The film conductivity values were obtained through the method of two coplanar contacts. According to the characteristics of the measurement system, the probe tips were 1.0 cm apart and 0.1 cm in diameter at the point of contact with the film. Aiming at determining the activation energy for electrical conduction in the films, Eq. C was used:

$$E_a = -\beta.k \qquad (C)$$

where, β is the angular coefficient of the curve ln(σ.T) by T^{-1}x10^3, E$_a$ (eV) is the activation energy, and k is the Boltzmann constant [8.62x10^{-5} eV/(atom.K)]. To measure the sheet resistance at room temperature, a head with four collinear tips was used on a multimeter with a current source. From the sheet resistance value, the electrical resistivity was calculated by:

$$\varrho = x.R_{sh} \qquad (D)$$

where R$_{sh}$ is the sheet resistance (Ω/□) and ϱ is the electrical resistivity (Ω.cm). A figure of merit (FOM) was used to optimize the electrical and optical properties of the films under analysis. It is a numerical expression used to characterize the materials' performance or devices in relation to others of the same type. The Eq. E correlates the two most significant parameters for the operation of absorbing layers in photovoltaic conversion, the absorption coefficient (α) and resistivity (ϱ) [6]:

$$F = \frac{\alpha}{\rho} \qquad (E)$$

where F is the figure of merit. Structural characterization was conducted using an X-ray diffractometer (XRD-7000, Shimadzu) under CuKα radiation (λ=1.5406 Å), continuous scan range in 2θ starting at 10° until 62°, with a speed of 4 °/min. The diffracted intensities obtained were normalized (relative to 100%) and the graphics were arranged in a Y-offset layout, i.e., one above the other to ease comparison [12]. By comparing the reference X-ray diffraction (XRD) patterns with the measured XRD pattern of each solute used, PbI$_2$ and PbBr$_2$, it was possible to investigate whether there was a total conversion of the solution components into the perovskites MAPbI$_3$ or MAPbBr$_3$. Thus, it was possible to identify the crystalline structure and phases present in the films and calculate the crystallite size (D$_{hkl}$) by Scherrer equation, using the highest intensity peak, according to [13]:

$$D_{hkl} = k_0 \frac{\lambda_i}{B_{hkl} . \cos(\theta_{hkl})} \qquad (F)$$

where k$_0$ is a constant with a value of 0.9, λ$_i$ is the incident radiation wavelength (1.5406 Å), B$_{hkl}$ is the peak width at half height (FWHM), and θ$_{hkl}$ is the Bragg diffraction angle of the highest intensity peak.

RESULTS AND DISCUSSION

The experiments comprised twenty depositions, ten for MAPbI$_3$ and ten for MAPbBr$_3$, denoted from 1 to 10 and labeled A and B, respectively. The deposition temperature and precursor solution flow rate were varied and are presented in Table I, along with the corresponding film thicknesses which ranged from 1.67 to 5.37 μm. Fig. 1 presents the cross-sectional image of sample A4 taken via confocal microscopy. It serves as an illustrative example of how thickness was measured. The micrograph

Table I - Deposition parameters of MAPbI$_3$ (A) and MAPbBr$_3$ (B) films deposited by ASP and their thickness.

Sample A/B	Deposition temperature (°C)	Solution flow (mL/min)	Thickness A (μm)	Thickness B (μm)
1	250	0.25	3.35	2.62
2	250	0.50	5.37	3.02
3	300	0.25	2.75	2.01
4	300	0.50	4.56	2.35
5	300	0.75	5.03	2.68
6	350	0.25	1.68	1.67
7	350	0.50	2.01	2.00
8	350	0.75	3.69	2.55
9	400	0.50	1.67	1.68
10	400	0.75	1.85	2.35

clearly demonstrates a distinct division between the film and substrate. The lower and thicker portion in light gray corresponds to the glass substrate, while the upper and darker part in dark gray represents the deposited film. This micrograph pattern was consistently observed across all samples to determine their respective thicknesses. As indicated in Table I, the pairwise analysis of the results, where one variable parameter was fixed and the other was modified, confirmed the expected logic. Particularly, as the deposition flow rate increased, the film thickness also increased due to the greater amount of material reaching the substrate. Raising the substrate temperature reduced the film thickness because of a decrease in precursor solution volume reaching the substrate surface due to an intensified temperature gradient. Moreover, increasing the substrate temperature may have exceed the optimal temperature range for the formation of dense, adherent, and smoother films by causing residual solvent evaporation, droplet spreading, and precursor salt decomposition on the substrate surface, as proposed by Parednis et al. [16]. It is also noted that, under the same deposition conditions (samples 3 and 4), the iodine films were thicker than the bromine ones.

In terms of morphological characterization, topographic images indicated the presence of circular shapes in all samples deposited at 250 °C, indicating dripping, as illustrated in Fig. 2. This suggested that this temperature was inefficient for the pyrolysis of the precursor solution, as the expected vapor phase was not formed, and the solution fell onto the substrate in the form of droplets. Films A5 (highlighted), A6, A7, A8, A9, A10, and B5 showed discrete microcracks, as shown in Fig. 3. Furthermore, it is worth noting that there was partial coverage in samples A9 and A10, and the analysis focused on the region where visual film deposition was observed. Samples A3, A4, B3, B4, B6, B7, B8, B9, and B10 displayed a favorable morphology, devoid of any cracks, and uniformly adhered to the substrate, as shown in Fig. 4. Therefore, their properties were studied in detail and are presented below.

Regarding the optical characterization, Fig. 5 shows the transmittance curves as a function of the wavelength of the films with the best morphological performance. Upon analyzing the films deposited at 300 °C (Fig. 5a), within the visible spectrum region at 700 nm, it was found that the MAPbI$_3$ film A3 exhibited the highest optical transmittance value of 22.12%. Among the MAPbBr$_3$ films, the sample B3 demonstrated the highest transmittance value, reaching 84.07%. When comparing all pairwise cases, including the remaining bromine samples from B6 to B10 (Fig. 5b), a clear
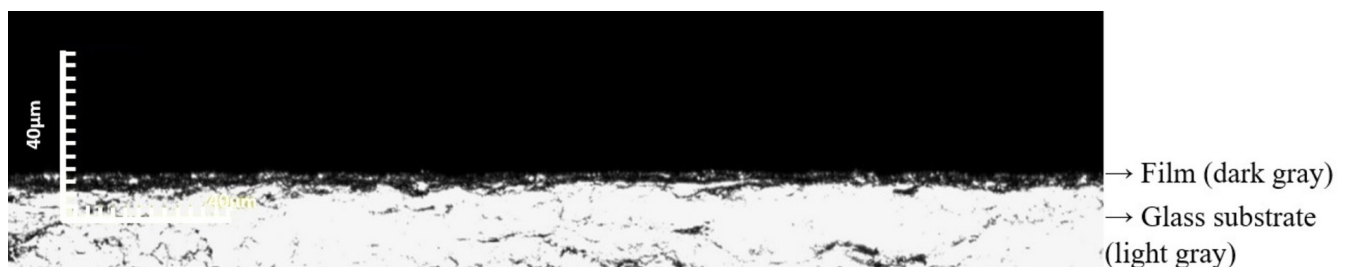

Figure 1: Cross-sectional micrograph of sample A4 revealing the dark gray region (perovskite film) and a lighter region (glass substrate).

→ Film (dark gray)
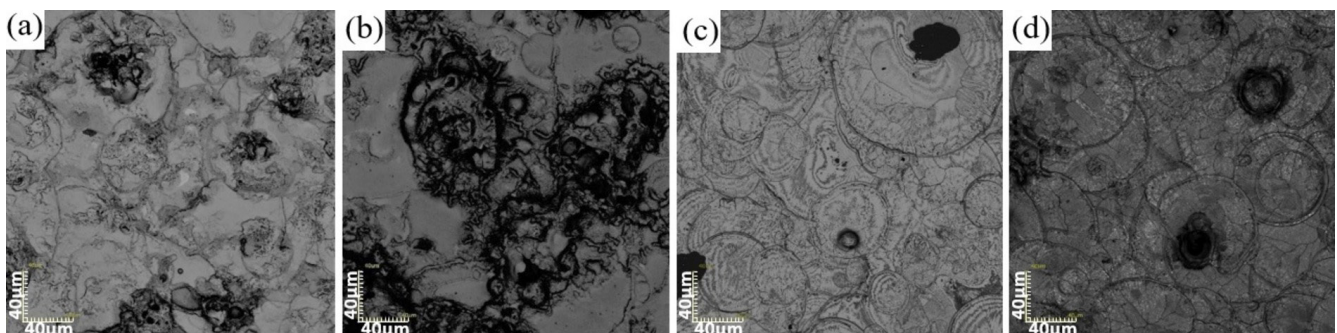→ Glass substrate (light gray)

Figure 2: Top-view micrographs of samples A1 (a), A2 (b), B1 (c), and B2 (d) showing some circular precursor solution dripping marks.
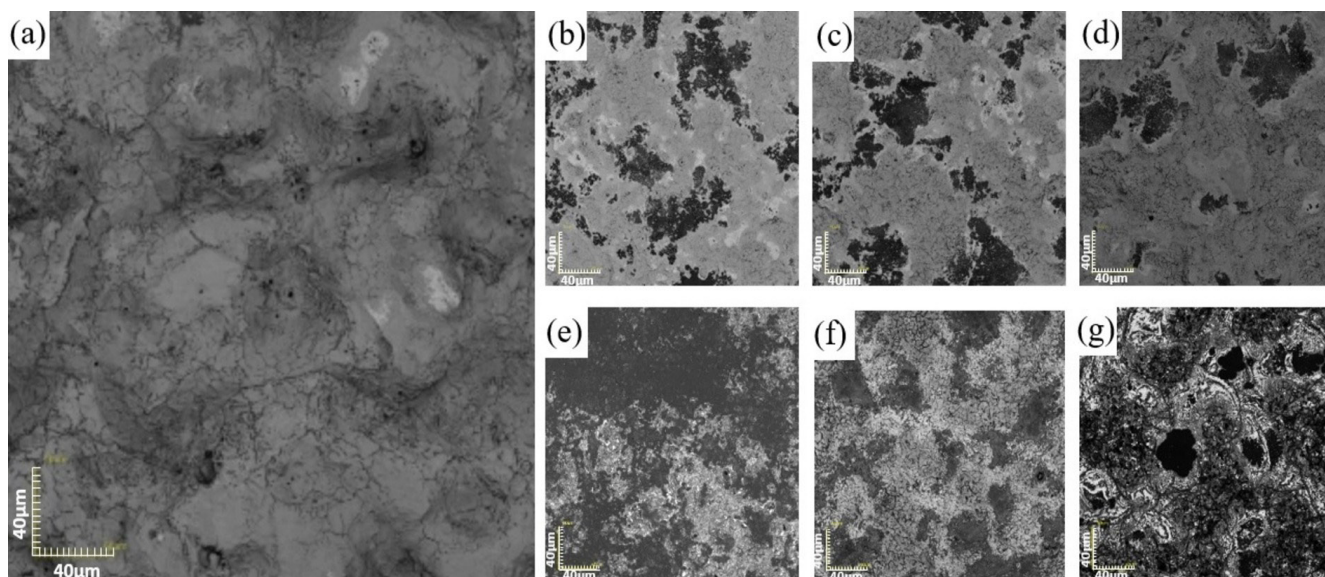
Figure 3: Top-view micrographs of samples A5 (a), A6 (b), A7 (c), A8 (d), A9 (e), A10 (f), and B5 (g) showing microcracks along the entire surface.
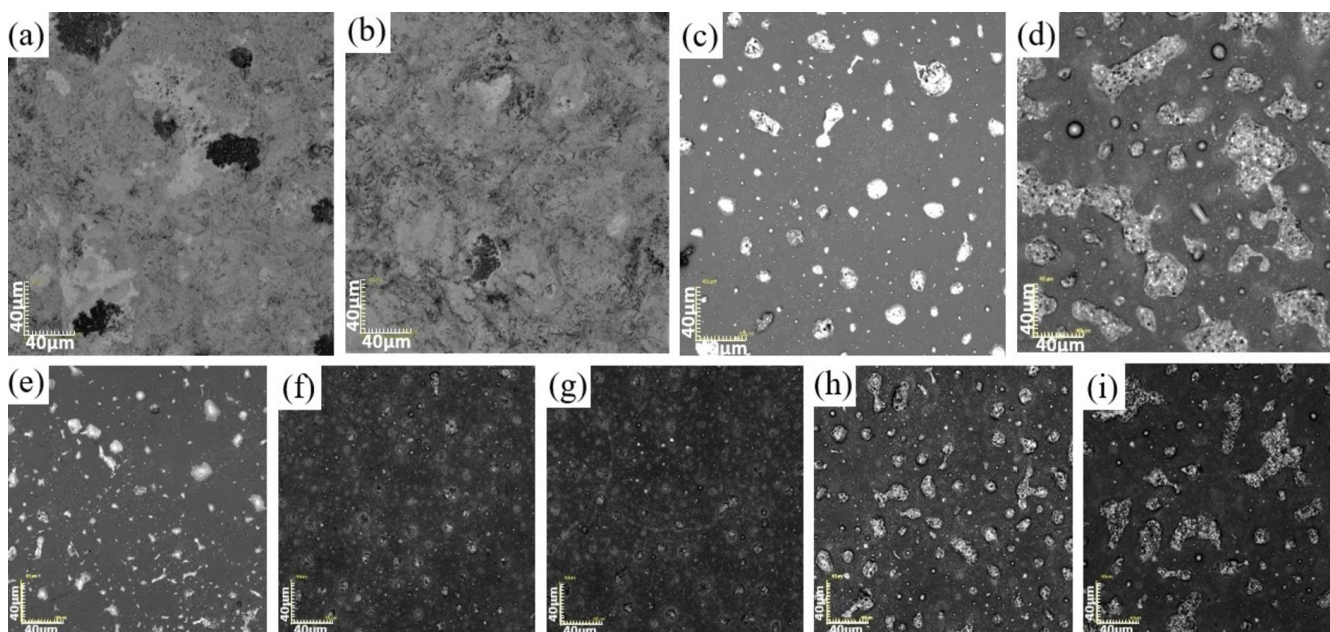

Figure 4: Top-view micrographs of samples A3 (a), A4 (b), B3 (c), B4 (d), B6 (e), B7 (f), B8 (g), B9 (h), and B10 (i).

trend emerges where the optical transmittance decreased as the film thickness increased. This can be attributed to the greater amount of material reaching the substrate due to an increased solution flow. As a result, less light is transmitted through thicker films, and more light passes through thinner ones. It was also observed that MAPbBr$_3$ films had higher transmittance values than those of MAPbI$_3$. Although visual analyses are not quantitative, it was noticeable that B films were more transparent than A films. The thickness obtained during the morphological characterization confirmed that films composed of bromine were less thick than those of iodine, therefore transmitting more light. As indicated in Table II, the optical absorption coefficient (α) underwent little alteration with parameter variations. However, there

was a reduction in α from A to B, indicating the superiority of MAPbI$_3$. It is noteworthy that sample A4, with an optical absorption of 0.58×10^4 cm^{-1}, surpassed the literature α value of 0.50×10^4 cm^{-1} for a MAPbI$_3$ film [17]. Therefore, the film deposited at 300 °C and at a flow rate of 0.50 mL/min is very promising for producing high-efficiency photovoltaic cells.

Fig. 6 presents a Tauc plot to determine the energy gap (Eg) obtained by linear extrapolation of A3 and A4 curves. This methodology was applied to all samples. According to Table II, sample A4 corroborated the bandgap value reported in the literature for MAPbI$_3$, which is 1.50 eV [18], while sample A3 exhibited a value close to the reference being 1.55 eV. Considering the reference bandgap value of 2.36 eV for MAPbBr$_3$ [6], it can be inferred that samples
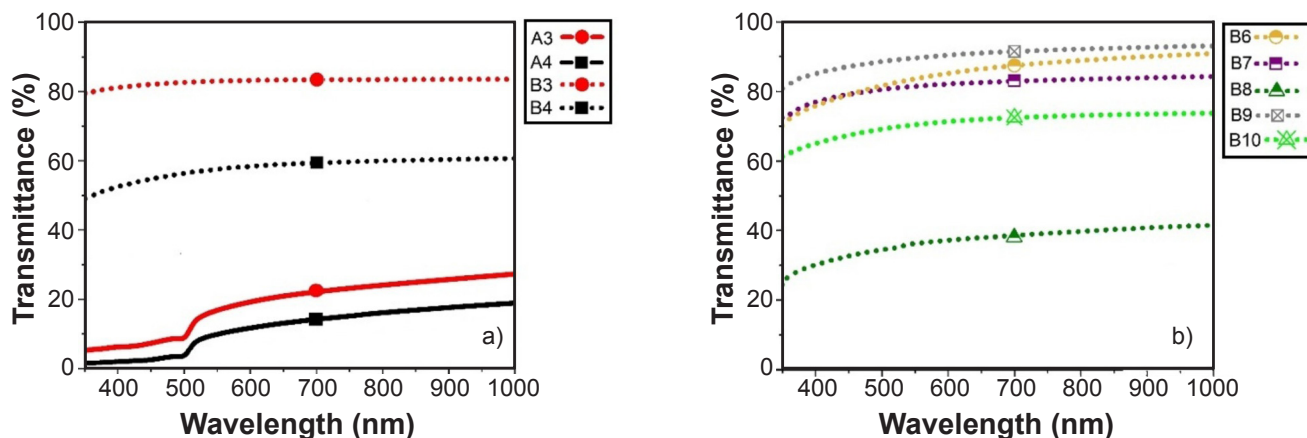
Figure 5: Optical transmittance as a function of wavelength, with reference at 700 nm for: a) MAPbI$_3$ and MAPbBr$_3$ samples deposited at 300 °C; and b) MAPbBr$_3$ samples.

Table II - Absorption coefficient (α) and optical gap (E$_g$).

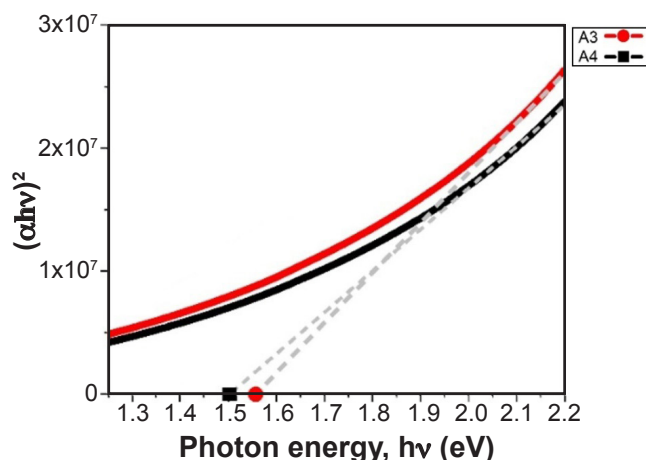| Sample	α (cm^{-1})	E$_g$ (eV)
A3	0.57x10^4	1.55
A4	0.58x10^4	1.50
B3	0.27x10^4	2.40
B4	0.50x10^4	2.33
B6	0.40x10^4	2.39
B7	0.34x10^4	2.45
B8	0.30x10^4	2.80
B9	0.19x10^4	1.90
B10	0.22x10^4	2.00

Figure 6: Tauc plot, $(\alpha h\nu)^2$ versus photon energy (hν), for obtaining the bandgap (E$_g$) through linear extrapolation (represented by the dashed gray line).

B3, B4, and B6 had approximate values compared to the literature, specifically 2.40, 2.33, and 2.39 eV, respectively [6]. Consequently, the following results are focused on these samples.

Regarding the electrical characterization, Fig. 7a presents the linear representation curves of the product of electrical conductivity and temperature variation [ln(σ.T)] as a function of inverse temperature (1000/T) of the best-ranked morphological and optical samples (A3, A4, B3, B4, and B6). It was observed that all films behaved as semiconductors [1, 2, 3, 6], as the electrical conductivity increased continuously with increasing temperature. According to Table III, the linear regression coefficient (R) was close to 1, meaning there was only one activation energy (E$_a$) within the temperature range analyzed. It exhibited slight variation among the investigated deposition conditions. This activation energy is associated with ionic migration which dominates the total conductivity and increases exponentially according to the Nernst-Einstein equation. The obtained E$_a$ values were consistent with those reported for MAPbI$_3$ [19]. Fig. 7b presents the average values of sheet resistance (R$_{sh}$) with error bars, while Table III contains the corresponding electrical resistivity values. It can be observed that the MAPbBr$_3$ samples were slightly less conductive than the iodine ones, with generally slightly higher electrical

resistivity, which is consistent with the results analyzed and calculated here. The error bars indicated the homogeneity of the samples; larger error bars would indicate greater variation in the measured values across different positions, and hence a more heterogeneous morphology. The samples with smaller error bars were A4 and B4. The figure of merit (FOM) for the best morphological, optical, and electrical samples is presented in Table III. It is noteworthy that A4 and B4 films achieved the highest FOM values, with A4 exhibiting slightly higher values than B4.

Regarding the structural analysis, Figs. 8a and 8d display the X-ray diffraction (XRD) patterns of the PbI$_2$ and PbBr$_2$ powders used in the precursor solutions, respectively. These patterns were compared with the XRD patterns of the deposited films [14] to check for the presence of unconverted solutes. All analyzed samples exhibited a characteristic orthorhombic polycrystalline structure. For lead iodide, according to the file JCPDS 00-046-1836, the four main peaks were indexed in decreasing order of intensity, being located at 25.96°, 34.32°, 39.50°, and 12.70° corresponding to the planes (001), (012), (110), and (001). It is observed in
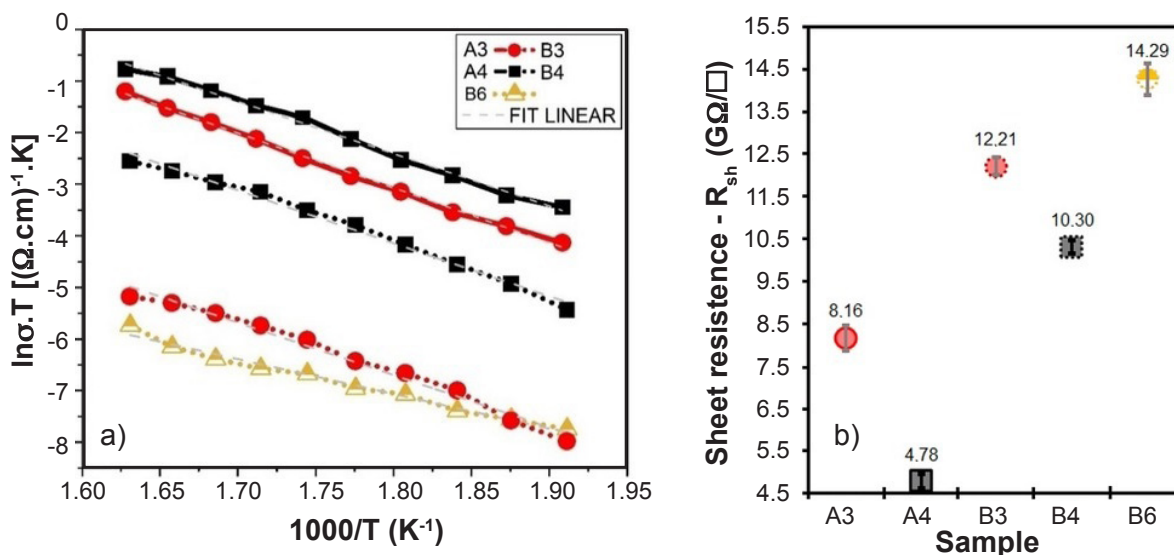
Figure 7: Graph illustrating the relationship between the electrical conductivity-temperature product and the inverse temperature of the heating base in a two-point electrical characterization system (a), and the average sheet resistance with error bar (b) of the samples with the best morphological and optical performances.
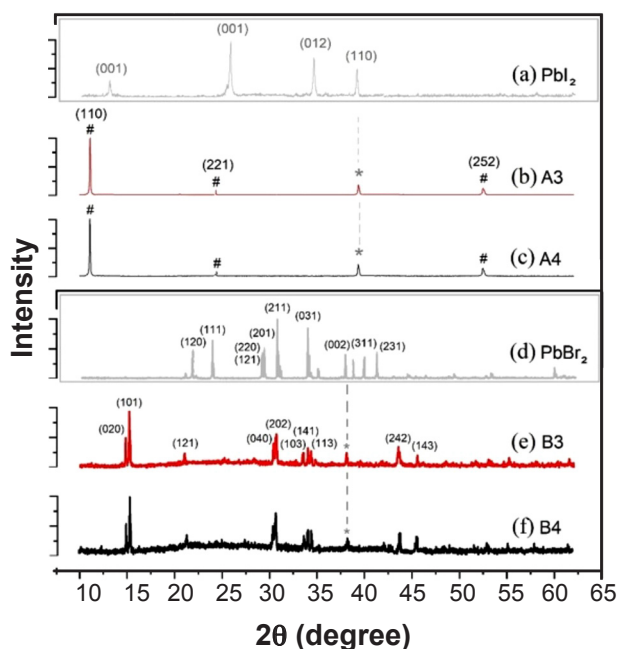

Figure 8: XRD patterns of the samples: a) PbI$_2$ (powder); b) A3; c) A4; d) PbBr$_2$ (powder); e) B3; and f) B4 (* - unconverted solute peak; # - peak of the desired perovskite phase).

Table III - Activation energy (E$_a$), linear regression coefficient (R), electrical resistivity, and figure of merit of selected samples.

Sample	E$_a$ (eV)	R	Resistivity (kΩ.m)	Figure of merit
A3	0.91	0.99	22.44	2.54
A4	0.87	0.99	21.80	2.66
B3	0.88	0.99	24.54	1.10
B4	0.87	0.99	24.20	2.07
B6	0.87	0.98	22.40	1.68

respectively (Fig. 8d). It is observed in Figs. 8e and 8f that B3 and B4 samples showed the same indexed peaks as the desired perovskite. According to the file JCPDS 01-076-2758, ten points of decreasing intensity were identified at 15.14°, 14.98°, 30.60°, 43.50°, 30.16°, 33.94°, 21.36°, 34.22°, 33.30°, and 45.54°, corresponding to planes (101), (020), (202), (242), (040), (141), (121), (113), (103), and (143). Both PbBr$_2$ and MAPbBr$_3$ had many peaks and some of them basically overlapped when compared. However, what differentiated them was their height (intensity). All samples exhibited a peak of unconverted solute, denoted by *. However, the perovskite's first peaks with greater intensity in the films suggested satisfactory conversion results. This indicated that only a small amount of powder precipitated after solvent mixing time, leading to the belief that the reported agitation time or intensity was insufficient. Some authors [18], for instance, stir the solution dissolved in γ-butyrolactone (GBL) overnight at 60 °C.

Crystallite sizes were calculated for the best-performing samples of MAPbI$_3$, the A3 and A4 samples. The peak of greatest intensity was the same for both A3 and A4 samples, at 2θ=10.75°. The largest crystallite size was found in A3 with 85.1 nm, while the smallest was in A4 with 81.7 nm.

Figs. 8b and 8c the A3 and A4 films did not show significant differences in the XRD patterns. The peaks were indexed in decreasing order of intensity, being located at 10.74°, 24.10°, and 52.50° corresponding to planes (110), (221), and (252) of the perovskite phase, respectively.

For lead bromide, according to file JCPDS 00-031-0679, the ten main peaks were indexed, which, in decreasing order of intensity, were located at 30.50°, 33.92°, 23.74°, 21.60°, 29.06°, 40.82°, 28.94°, 28.74°, 37.98°, 39.64°, and 38.42°, corresponding to planes (211), (031), (111), (120), (201), (231), (220), (120), (002), (311), and (320),

Similarly, for MAPbBr$_3$ samples, the most intense peaks were observed at 2θ=15.15°. The largest crystallite size was found in the B3 sample at 84.0 nm, and the smallest in the B4 sample at 75.6 nm. There was not a significant variation in crystallite size under the investigated parameters, and the values were within the range of a few tens of nanometers. This size is advantageous since smaller crystallites are not suitable for radiation-absorbing layers in solar cells due to the high density of grain boundaries, which act as recombination centers for the photogenerated charge carriers [20].

CONCLUSIONS

The choice of the deposition parameters for automated spray-pyrolysis (ASP) systems is a factor that influences the morphological, optical, electrical, and structural properties of the MAPbI$_3$ and MAPbBr$_3$ layers. The surfaces of MAPbI$_3$ samples deposited for 5 min at a deposition temperature of 300 °C and deposition flow rates of 0.25 and 0.50 mL/min exhibited a continuous and homogeneous appearance. In contrast, a greater number of MAPbBr$_3$ samples showed improved results in terms of topographic analysis. The optimal parameters for these samples at the 5 min deposition time were deposition temperatures of 300, 350, and 400 °C, and precursor solution flow rates of 0.25, 0.50, and 0.75 mL/min. All analyzed samples can be considered light absorbers although the iodine-based samples demonstrated a slightly higher absorption coefficient compared to those reported in the literature. It is also inferred that all films deposited had semiconductor characteristics, exhibiting only one activation energy for each curve, within the temperature range analyzed. Iodine samples were slightly more conductive than bromine ones. Resistivity, being an intrinsic characteristic of the material, fluctuated little for samples with slightly higher bromine values than iodine, corroborating the conductivity curves. XRD analysis evidenced the formation of polycrystalline orthorhombic perovskites. The figure of merit analysis showed that the best results were obtained for the MAPbI$_3$ and MAPbBr$_3$ films deposited for 5 min at 300 °C, using a flow rate of 0.50 mL/min, at 30 cm from the atomizing nozzle. These conditions were applied under a pressure of 0.50 kgf/cm² of carrier gas and a concentration of 0.025 M. The results obtained and presented in this paper demonstrated the feasibility of producing MAPbI$_3$ and MAPbBr$_3$ films for use as absorber layers in solar cells, using the ASP technique and highlighting the simplicity and efficiency of this deposition technique.

ACKNOWLEDGMENTS

REFERENCES

[1] A. Wang, C. Zuo, X. Niu, L. Ding, J. Ding, F. Hao, Chem. Eng. J. **451**, 4 (2023) 138926.
[2] A. Kojima, K. Teshima, Y. Shirai, T. Miyasaka, J. Am. Chem. Soc. **131** (2009) 6050.
[3] D. Lin, Z. Zhan, X. Huang, P. Liu, W. Xie, Mater. Today Adv. **16** (2022) 100277.
[4] U. Rani, P.K. Kamlesh, R. Agrawal, A. Shukla, A.S. Verma, Energy Technol. **10** (2022) 2200002.
[5] U. Rani, P.K. Kamlesh, R. Agarwal, J. Kumari, A.S. Verma, Int. J. Quantum Chem. **121** (2021) e26759.
[6] P. Roy, N.K. Sinha, S. Tiwari, A. Khare, Sol. Energy **198** (2020) 665.
[7] Y. Zhang, P. Cheng, W. Tan, Y. Min, Appl. Surf. Sci. **537** (2021) 147908.
[8] C.S. Manhanini, H.R. Paes Jr., Cerâmica **63**, 366 (2017) 233.
[9] A.E. Alves, H.R. Paes Jr., Exatas Eng. **10** (2020) 1.
[10] O.P. Rocha, "Implementação de um sistema de spray-pirólise automatizado para deposição de filmes cerâmicos com gradiente de funcionalidade e dispositivos multicamadas", Dr. Thesis, Univ. Est. Norte Fluminense, Campos Goytacazes (2017).
[11] P. Nagarjuna, K. Narayanaswamy, T. Swetha, G.H. Rao, S.P. Singh, G.D. Sharma, Electrochim. Acta **151** (2015) 21.
[12] J.S.C. Licurgo, G.R. de Almeida Neto, H.R. Paes Junior, Cerâmica **66**, 379 (2020) 284.
[13] J. Tauc, A. Menth, J. Non-Cryst. Solids **8**, 10 (1972) 569.
[14] B.S. Swain, M.A.K. Sheikh, S. Singh, R. Abdur, D. Jeong, J. Lee, Mater. Sci. Semicond. Process. **74** (2017) 361.
[15] C.J. Panchal, V.R. Kheraj, J.R. Ray, M.S. Desai, Sol. Energy **83** (2009) 753.
[16] D. Parednis, O. Wilhelm, S. Pratsinis, L. Glaucker, Thin Solid Films **474** (2005) 84.
[17] N.G. Park, Mater. Today **18** (2015) 65.
[18] H. Kim, C. Lee, J. Im, K. Lee, T. Moehl, A. Marchioro, S. Moon, R. Humphry-Baker, J. Yum, J. Moser, M. Grätzel, N. Park, Sci. Rep. **2** (2012) 591.
[19] D. Liu, Q. Zhao, Z. Li, X. Sun, B. Zhang, Z. Shao, C. Chen, L. Hao, X. Wang, C. Gao, Y. Li, X. Wang, G. Cui, S. Pang, Solar RRL **6**, 9 (2022) 202200414.
[20] L.R. Cruz, Q.G.S. San Miguel, Matéria **17** (2012) 961.
(Rec. 16/03/2023, Rev. 12/06/2023, Ac. 27/07/2023)